Constructing an Anion-Braking Separator to Regulate Local Li^+ Solvation Structure for Stabilizing Lithium Metal Batteries

Zibo Zhang, Jian Wang,* Haozhe Qin, Bao Zhang, Hongzhen Lin, Weitao Zheng, Dong Wang,* Xiaobo Ji,* and Xing Ou*

ABSTRACT: **Lithium metal batteries (LMBs) offer significant advantages in energy density and output voltage, but they are severely limited by uncontrollable Li dendrite formation resulting from uneven Li^+ behaviors and high reactivity with potential co-solvent plating. Herein, to uniformly enhance the Li behaviors in desolvation and diffusion, the local Li^+ solvation shell structure is optimized by constructing an anion-braking separator, hence dynamically reducing the self-amplifying behavior of dendrites. As a prototypal, two-dimensional lithiated-montmorillonite (LiMMT) is blade-coated on the commercial separator, where abundant −OH groups as Lewis acidic sites and electron acceptors could selectively adsorb corresponding FSI^- anions, regulating the solvation shell structure and restricting their migration. Meanwhile, the weakened anion mobility delays the time of breaking electrical neutrality, and the Li nucleation density is quantified through the respective experimental, theoretical and spectroscopical results, providing a comprehensive understanding of modifying anion and cation behaviors on dendritic growth suppression. As anticipated, a long Li plating/stripping lifespan up to 1800 h and a significantly increased average Coulombic efficiency of 98.8% are achieved under 3.0 mAh cm^{-2}. The fabricated high-loading Li-LFP or Li-NCM523 full-cells display the cycle durability with enhanced capacity retention of nearly 100%, providing the instructive guide towards realizing dendrite-free LMBs.**

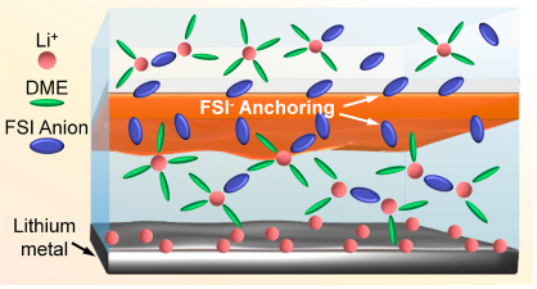

KEYWORDS: *lithium metal batteries, anion-braking effect, lithium dendrite, solvation shell structure, Li diffusion kinetics*

Aimed to satisfy the increasing demand for high-energy-density applications,[1,2] lithium metal anodes (LMAs) are famous for their high capacity (3860 mAh g^{-1}) and low potential (−3.04 V).[3−6] However, both the dendrite formation resulted from uncontrolled Li ion/atom diffusion kinetics and the failure of the solid electrolyte interphase (SEI) limit the commercialization of LMAs.[7−9] To deal with these issues, electrode host optimizations,[10−12] interface/surface engineering,[13−15] current collector construction and modifications,[16,17] electrolyte additives,[18−20] etc., have been created to decrease the local deposition current density to suppress the dendrites.[21] However, the essential elimination of the self-amplified growth of Li dendrites remains to be further explored when extending the plating capacity or current density.

Alternatively, a commercial polyethylene (PE) separator with the intrinsic mechanical and electrochemical stability has been used as an electrolyte reservoir for industrial-wide applications.[22−27] In a typical battery, the anion and cation diffusion contribute to the whole ionic conductivity (Figure 1a), but the anion is generally not involved in the delithiation/lithiation. However, the anion has a higher mobility compared to the larger Li(solvents)$^+$ solvated cluster (Figure 1a).[28] Meanwhile, the penetration of large solvated Li^+ behaviors across the separator is usually anisotropic, resulting in the heterogeneous nucleation and potential dendrite growth on the Li metal surface.[29,30] According to the Sand time equation[31]

$$\tau = \pi D \frac{eC_0(\mu_a + \mu_{Li^+})^2}{2j\mu_a} \quad (1)$$

for most studies, reducing the j (electrode current density) by constructing three-dimensional architectures is usually applied to increase τ (dendrite occurred time) to alleviate Li dendrite growth.[16,17] As observed above, the dendrite inhibition could

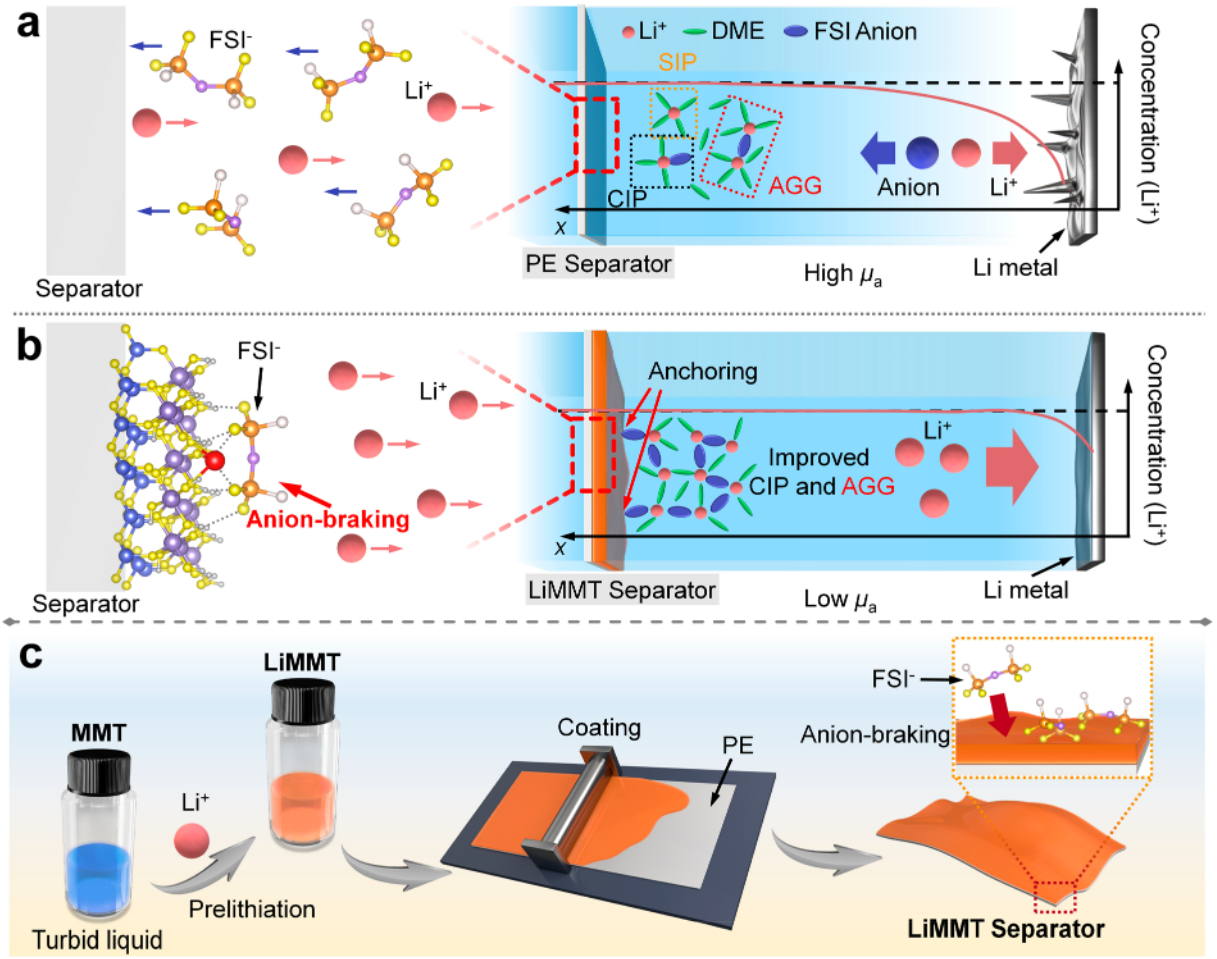

Figure 1. Schematic diagram of Li^+ transfer and electrodeposition with a (a) PE separator and a (b) LiMMT separator. (c) Schematic illustration of the preparation process of the LiMMT separator.

also be alleviated by increasing the t_{Li}^+ (Li transference number) to prolong τ.[25,32,33] Meanwhile, a higher μ_{Li}^+ helps to enhance the interfacial Li^+ concentration, which assists in the initial uniform nucleation in accordance with eq 1 (τ is increased along with boosting μ_{Li}^+).[34] Thus, a functionalizing separator is capable of significantly wetting the surface and affecting the Li plating/stripping behavior.[32,33,35−37]

As pointed, the Li plating behaviors have close relationships with interfacial electrolyte/electrode information evolution and corresponding Li(solvents)$^+$−anion solvation shell structures.[38] Previous studies point out that dissociating the Li^+ solvents rapidly could provide many bare Li^+ flux.[39,40] Meanwhile, regulating the anion-related solvation structure state could indeed improve the dissociation kinetics through constructing suitable pore engineering or active catalysts or electrolyte additives. However, for the behaviors of anions, there lies some embarrassing confusion toward dendrite inhibition: (1) a higher anion concentration is advantageous to the formation of anion-derived SEI,[41] and (2) a high μ_a promotes the concentrated polarization and Li dendrite self-amplification development, causing dissatisfactory side reactions and shortened cycling life.[42] From above, one can make sense that there is a "trade-off" between utilization and lifespan when introducing a high-concentration anion salts strategy. To further describe this phenomenon, an extended eq 2 in direct proportion to the τ is derived from eq 1 as follows:

$$(\mu_a + \mu_{Li^+})^2/\mu_a = \mu_a + \frac{\mu_{Li^+}^2}{\mu_a} + 2\mu_{Li^+} \quad (2)$$

As revealed, there exists no definite relevance between μ_a and τ, which further confirms the above contradiction. According to the law of ion migration, the sum of $\mu_a + \mu_{Li}^+$ is constant and equal to 1.[42,43] Therefore, an anion-philic functional separator with reduced anion mobility (μ_a) could enlarge the τ value with retarded dendrites by modulating the corresponding Li(solvents)$^+$ solvation shell, effectively inhibiting the self-amplified dendrite growth.

In this study, the Li(solvent)$^+$−anion solvation shell structure is modulated by constructing a domed anion-braking separator (Figure 1b). To verify our hypothesis, we propose a concept of anion-braking to decrease the μ_a to regulate the Li nucleation and plating in a lithium bis(fluorosulfonyl)imide (LiFSI) electrolyte, prepared by blading a commercial polyethylene (PE) separator with lithiated-montmorillonite (LiMMT) (Figure 1c). Due to its characteristics, coating LiMMT on the copper foil exhibits obvious achievements for LMAs.[44−46] Although the LiMMT has been reported on the metallic Li surface with modification, the corresponding investigations are mainly focused on lithium ion conductivity or its lithiophilic properties. The LiMMT in this work is selected as the demo to fully strengthen the concept of anion-braking for regulating Li^+ solvation behaviors, providing the

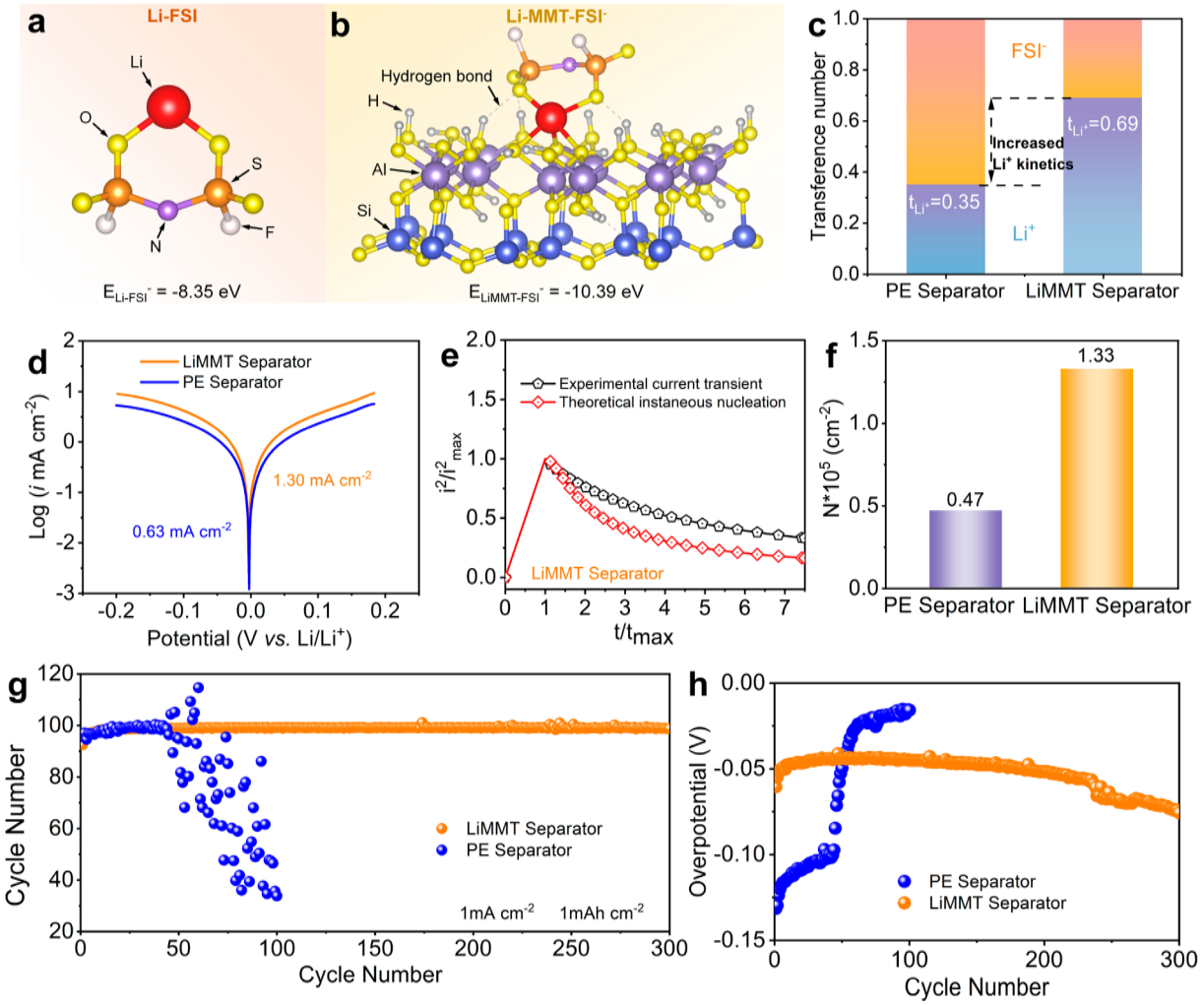

Figure 2. Binding energies of (a) Li-FSI⁻ and (b) LiMMT-FSI⁻ calculated by DFT. (c) Comparisons on the lithium ion transference number. (d) Tafel plots obtained from a CV test. (e) Dimensionless graphs of the current transients of Li deposition on Cu for the LiMMT separator. (f) Comparisons of nucleation density between the PE separator and LiMMT separator. (g) Coulombic efficiencies of LilCu cells with the PE separator or LiMMT separator with a Li deposition capacity of 1 mAh cm^{-2} and (h) corresponding overpotentials.

solid evidence on the positive effect of LiMMT for the anion control. Correspondingly, this functional lithiated-montmorillonite (LiMMT) layer selectively adsorbs and prevents the mobility of FSI$^-$ anions (μ_a), regulating the corresponding solvation shell structure with a lower barrier to release bare Li$^+$. Meanwhile, the effect of modulated ionic behavior on Li nucleation density (N_0) is analyzed. The μ_a reduced system constructed by the anion-braking effect of LiMMT prolongs the ion-depleted layer around the electrode, which facilitates the uniform distribution of Li$^+$ flux and reduces the concentration polarization, as revealed by experimental and theoretical results together with Raman and sum frequency generation spectroscopical measurements, providing a comprehensive understanding of modifying anion and cation behaviors on dendritic growth suppression. As expected, a long Li plating/stripping lifespan of up to 1800 h and significantly increased Coulombic efficiency are achieved under a high deposition capacity. The fabricated high-loading Li-LFP or Li-NCM523 full-cells display cycle durability with enhanced capacity retention.

RESULTS AND DISCUSSION

The fabrication of LiMMT is synthesized by ion-exchange reactions between commercial MMT and Li salts (Figure S1). The high-resolution transmission electron microscopy (HRTEM) reveals the slight lattice fringe change of the (103) crystal plan of MMT from 0.341 to 0.324 nm (Figure S2). The X-ray diffraction (XRD, Figure S3a) patterns record the slight layer change of the (001) crystal plane of MMT from 1.328 to 1.242 nm, suggesting the successful exchange of Li$^+$ with Ca^{2+}. Meanwhile, the lifting intensity of Li and corresponding reduction of Ca also demonstrated successful ion exchange for LiMMT (Figures S3b–S3d). Both Fourier transform infrared spectroscopy (FTIR) and the O 1s spectra of X-ray photoelectron spectroscopy (XPS) can display a relatively high consistency between MMT and LiMMT (Figure S4), indicating the reserved structure of MMT after Li ion exchange. Meanwhile, the peak at 1630 cm^{-1} assigned to the −OH group increases slightly, which might be attributed to the abundant −OH functional groups at the edge of LiMMT. After coating, the LiMMT modified separator reserves the mechanical property without obvious falling off when folded (Figure S5). In the scanning electron microscopy (SEM)

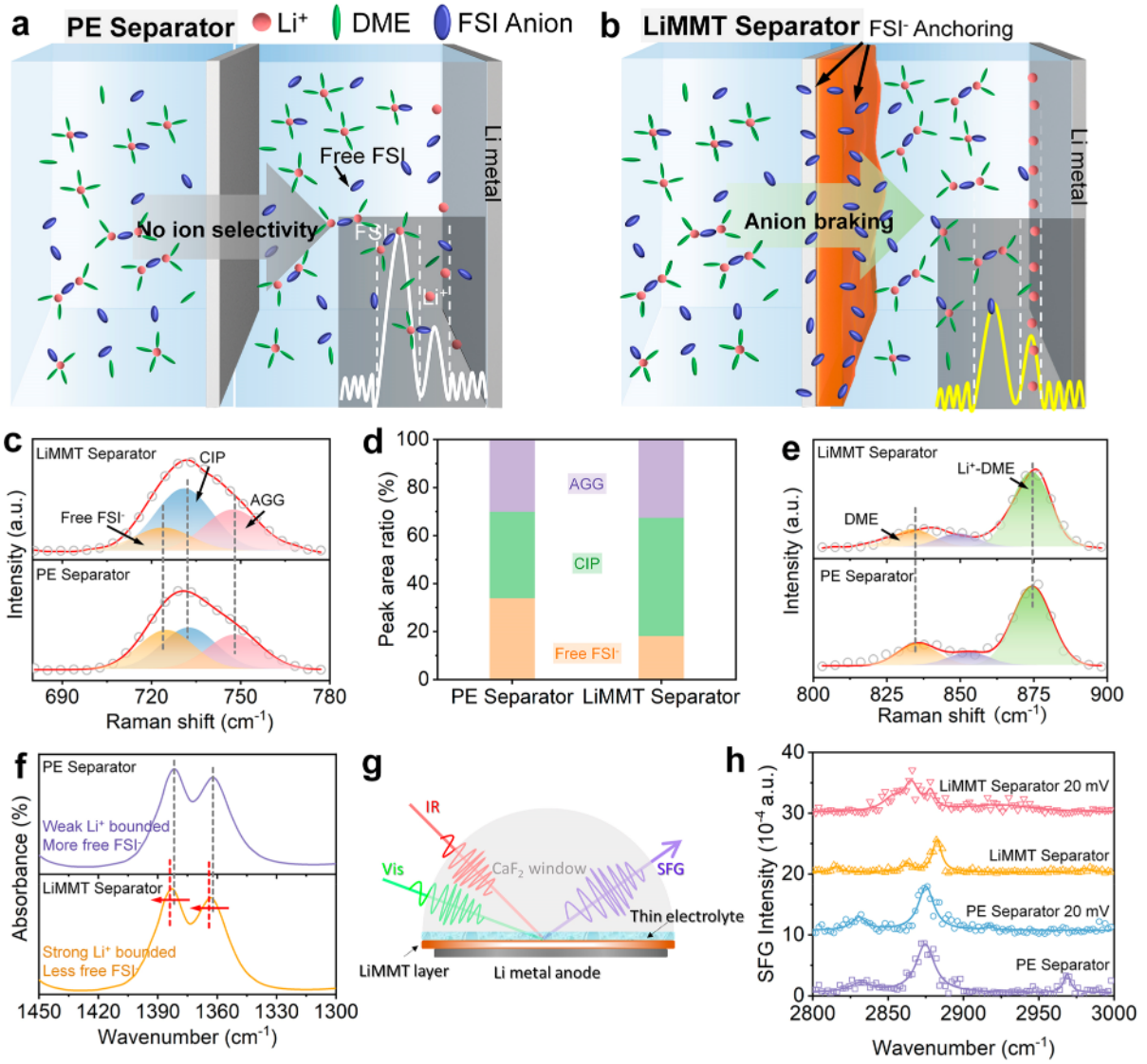

Figure 3. Schematic diagram of desolvation process with the (a) PE separator and (b) LiMMT separator. (c) Raman spectra of electrolytes with PE or LiMMT separators in 680−780 cm^{-1} and (d) the corresponding peak radio. (e) Raman spectra of electrolytes with PE or LiMMT separators in 800−900 cm^{-1}. (f) FTIR spectra characterization of the same electrolyte with different separators from 1300−1450 cm^{-1}. (g) Schematic illustration of the in situ SFG cell detecting the electrolyte/separator interface. (h) SFG spectra of different solvation structures with a PE or LiMMT separator under an OCV or a bias of 20 mV.

images, the morphology of the PE surface is completely changed from a porous structure to LiMMT flakes decoration, and the corresponding thickness of the LiMMT layer is about 2 μm (Figure S6). Moreover, the corresponding EDX mappings further confirmed that all elements are uniformly distributed (Figure S7).

As is well-known, the interfacial ion behaviors can affect the formation and physicochemical properties of the solid electrolyte interphase (SEI). Initially, the binding energies of Li^+-FSI^- and LiMMT-FSI^- anions were calculated, and the binding energy is increased from 8.35 to 10.39 eV after introducing LiMMT (Figures 2a and 2b). The enhanced anion adsorption ability is ascribed to the Al−OH functional group in LiMMT as Lewis acidic sites that restrict the movement of anions. Further, the peaks at 684.5 eV (F 1s) and at 528.3 and 531.5 eV (O 1s) are well assigned to LiF, Li_2O, and Li_2CO_3 after plating, respectively (Figure S8).[47] The anion mobility (μ_a) is a widely used index to witness the carrier transport accompanied by the anion and cation transference number ($t_{Li}^+ + t_{anion}^- = 1$). As measured by the Bruce−Vincent method (Figure S9), the t_{Li}^+ in the commercial PE separator system is 0.32 (Figure 2c), which is mainly due to the insufficient free ions (Li^+, FSI^-). In sharp contrast, the t_{Li}^+ in the optimized LiMMT system is increased to 0.63 (Figure 2c), nearly two times higher than the commercial one. Even compared to other reported separators (Figure S10), an effective improvement for reducing μ_a (increasing t_{Li}^+) is exhibited, confirming the advantages of LiMMT in anion-braking and Li^+ acceleration.

The electrolyte wettability on the PE or LiMMT-decorated separators is recorded; as displayed, it is instantly wetted with a negligible contact angle in the LiMMT separator system (Figure S11, bottom), while the electrolyte droplet remains on the PE separator (Figure S11, upper). This superior electrolyte wettability of the LiMMT layer facilitates the uniformity of Li^+ flux, thereby alleviating the inhomogeneity of Li^+ transport.[48,49]

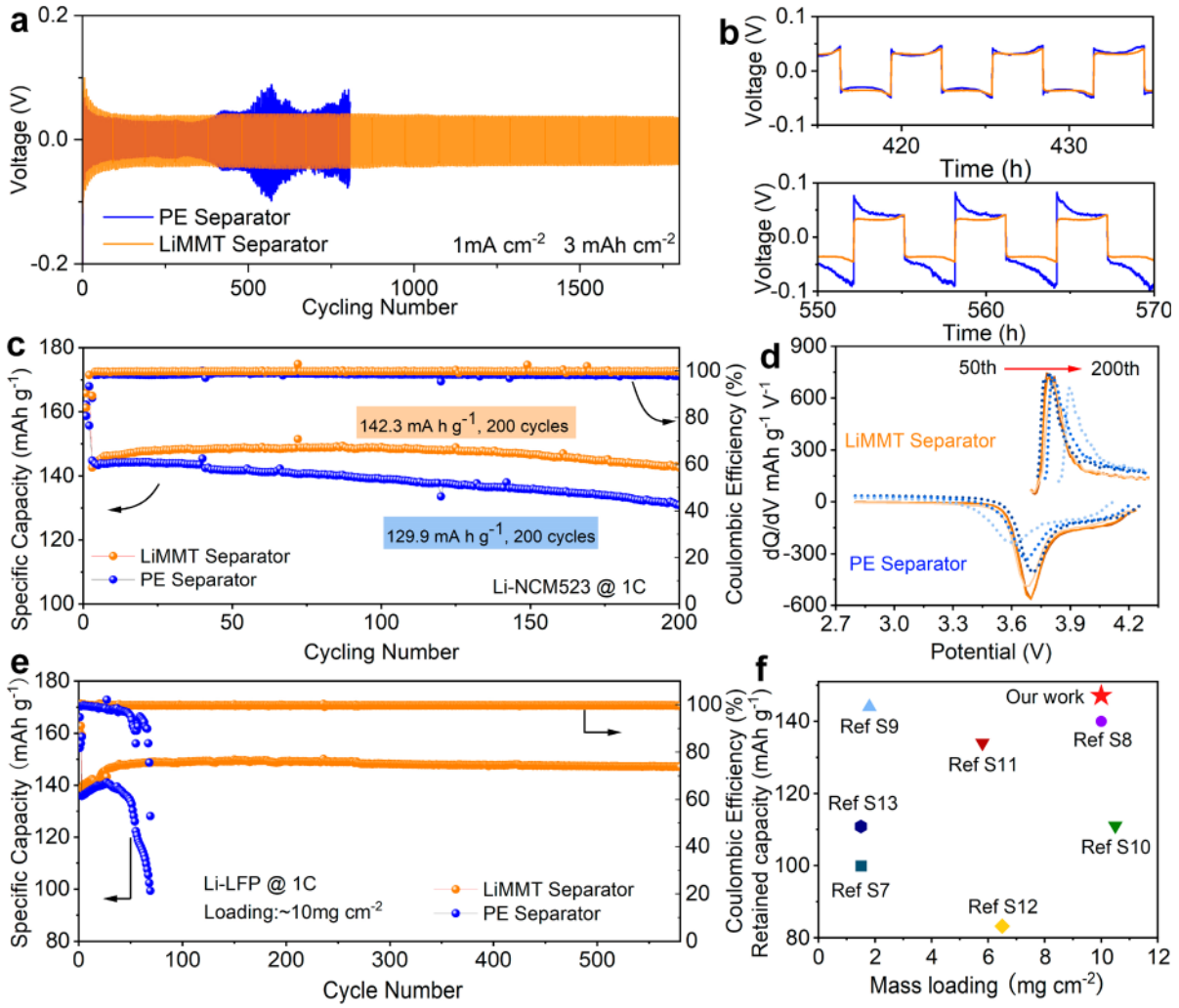

Figure 4. (a) Galvanostatic cycling profiles of symmetric cells based on a PE or LiMMT separator at 1 mA cm^{-2} under a practical capacity of 3 mAh cm^{-2}. (b) Comparisons on enlarged voltage curves for the PE and LiMMT separators. (c) Cycling performance and (d) the corresponding dQ/dV curves of the Li|NCM523 cells with PE and LiMMT separators at 1 C. (e) Cycling performances of the Li|LFP cells with PE and LiMMT separators at 1 C. (f) Comparison of our design with other reported Li metal batteries in terms of mass loading and retained capacity. References in the figure are provided in Table S1.

Roughly estimated (Figure S12), the Li^+ transport barriers (E_a) decrease from 13.73 to 7.32 kJ mol^{-1} after the introduction of LiMMT, indicating the lower energy barrier to overcome to accelerate Li^+ dissociation.[50] Furthermore, in the Tafel curve, the exchange current density is only ~0.63 mA cm^{-2} in the PE separator system, much lower than that in the LiMMT system (1.3 mA cm^{-2}), suggesting tardy deposition kinetics (Figure 2d). The nucleation barrier is as low as 46 mV when the Li^+ transfers across the electrode/electrolyte interface, boosting the uniform plating kinetics (Figure S13). Meanwhile, the restricted anion movement facilitates the reduction of the space charge layer and maintains the electroneutrality, thus eliminating the growth of Li dendrites. In order to investigate the effect of the anion-braking phenomenon on the Li nucleation/growth behavior, dimensionless analyses of Li deposition behaviors with/without LiMMT (obtained from Figure S14) are exhibited in Figure 2e and Figure S15, respectively. The 3D transient nucleation model fits the experimental curves better, demonstrating that Li nucleation growth follows the 3D instantaneous nucleation model. In this model, the active nucleation density (N_0) can be calculated directly from the current transients. Figure 2f shows a significant increase in nucleation density with the LiMMT one, which is beneficial for the dense Li deposition.

To evaluate the effectiveness and stability of LiMMT on Li plating/stripping, the Li|Cu cell with a LiMMT separator exhibits a steady average Coulombic efficiency (CE) of 99% with stable voltage profiles for 300 cycles (Figure 2g). On the contrary, the cell with the PE separator displays poor cycling stability with severe voltage fluctuations and CE tendencies (Figure 2h and Figure S16), falling down to around 33% after 100 cycles. Enhanced to 3 mAh cm^{-2} (Figure S17), the cell with LiMMT still maintains an average CE of 98.8% after 120 cycles, which is much longer than the commercial one. These results demonstrate that the LiMMT acts as a Li promotor, further confirming the utility of limited anion migration.

The desolvation process at the interface plays a major factor in improving the performance of LMBs as it is related to the kinetics of Li ions. Owing to the porous structure of separators, free anions and solvents without any dissociation alter and dominate in the inner Helmholtz plane (IHP) near the Li metal surface, resulting in sluggish Li^+ diffusion kinetics and

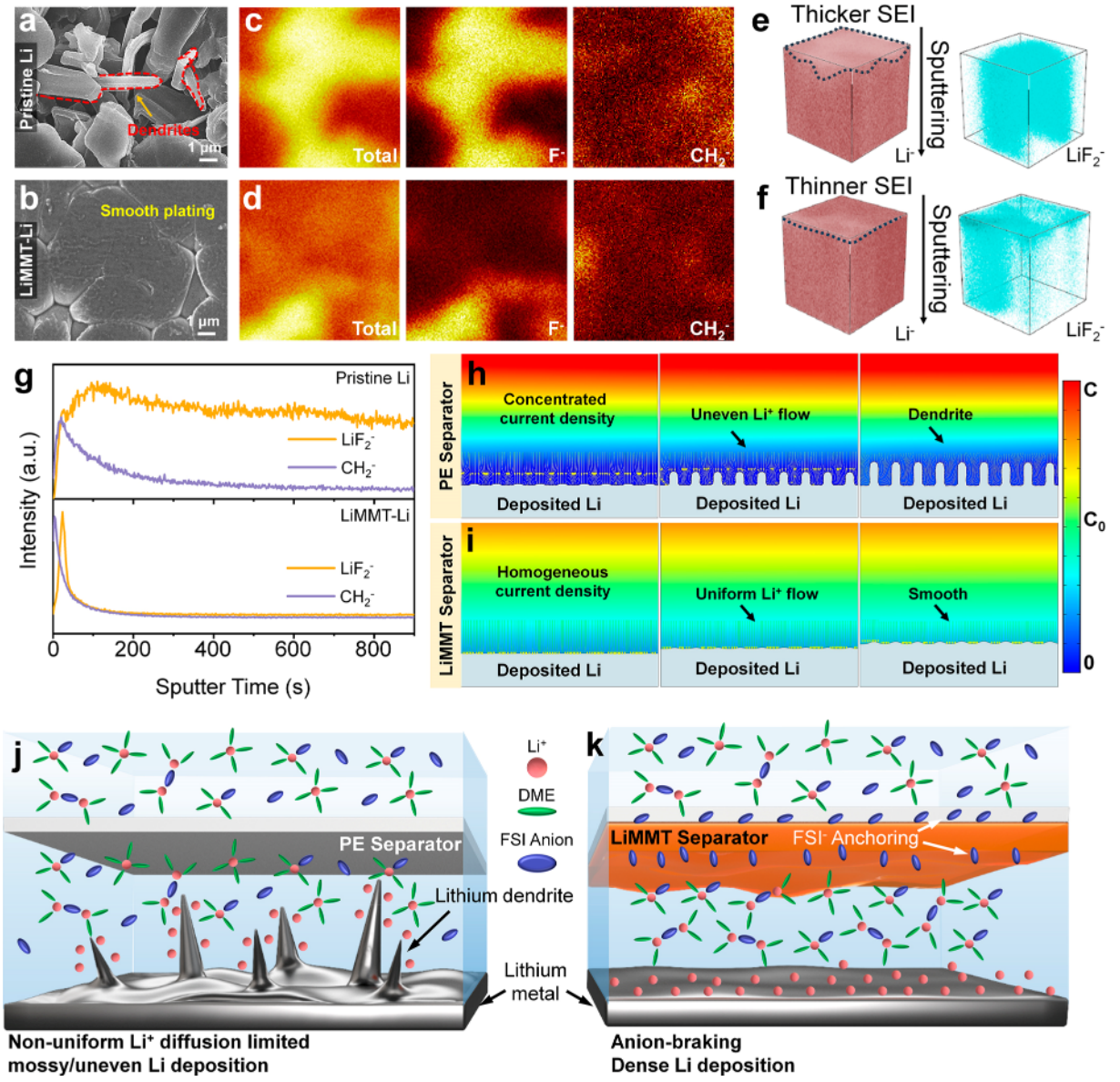

Figure 5. Top-view SEM image of Cu foil after Li deposition with 3 mAh cm^{-2} in the deposited state for the (a) PE separator and (b) LiMMT separator. ToF-SIMS chemical maps of second ion fragments with ~50 μm of sputtering in the lithium metal electrodes cycled in the (b) PE and (c) LiMMT separators and 3D reconstruction map in the (e) PE and (f) LiMMT separators. (g) Corresponding intensity sputter profiles measured by ToF-SIMS. Simulation results of Li deposition morphology, Li^+ concentration distribution, and electric field distributions for commercial (h) PE separators and (i) LiMMT separators over time. As the deposition time increases, cells with PE separators lead to increased concentration polarization, uneven current density distribution, and the Li self-amplifying dendrite growth. The cells with LiMMT separators show optimized results. Schematic illustration of the Li^+ deposition process with a (j) PE separator and a (k) LiMMT separator.

heterogeneous distribution of Li ions (Figure 3a). However, owing to the strong anion adsorption ability of LiMMT toward FSI^-, the solvation shell structure may be altered in the corresponding IHP. More contacted ion pairs and aggerates may possibly be formed with the restriction of anions (FSI^-) (Figure 3b). In order to confirm and gain more insights of the anion-braking behaviors in modulating solvation shell structure, the FTIR, Raman, and SFG spectroscopies are carried out. Three peaks at ~720 (orange region), 730 (blue region), and 740 cm^{-1} (pink region) are attributable to free FSI^-, CIP (one FSI^- and one Li^+ interaction), and AGG (one FSI^- coordinated with two Li^+) (Figure 3c), respectively. As acknowledged, the total ratios of CIP and AGG show the desolvation degree of $Li(solvent)^+$ species. The percentages of CIP and AGG account for (49% + 32%) in the LiMMT system, which is higher than that in commercial PE (36% + 30%) (Figure 3d). This implies that the LiMMT separator has a braking effect on the anions and reduces the free anions in the interface, which favorably minimizes the distribution of free anions in the IHP and promotes the distribution of Li ions on the Li metal surface. In addition, the influence of anion-brake behaviors can also be observed from the aspect of solvent coordination, and the formation of ion aggregates also reduces the degree of free solvent in the solvation shell (Figure 3e). Furthermore, the peaks in FTIR at around 1385 and 1365 cm^{-1} are attributed to the Li^+-FSI^- interaction and free FSI^-,

respectively (Figure 3f). Obviously, there are two different solvation states (Li^+ bounded state and free FSI^-). For the PE separator, there are more free FSI^-. In sharp contrast, the opposite results can be observed in the LiMMT separator with less free FSI^-. Also, the peak around 1075 cm^{-1} corresponds to its solvation; with the LiMMT separator, the change in intensity is evident and the sharp decrease of the Li^+-FSI^- interaction explains the reduction of free anions (Figure S18).

To further investigate the interfacial information, interface-selective sum frequency generation (SFG) spectroscopy is used to analyze the desolvation behaviors at the molecular level, as depicted in Figure 3g. Figure 3h evidences the $Li(solvent)^+$, i.e., $Li(DME)_4^+$, and the related adsorbed DME molecules at the interface with/without LiMMT under open-circuit voltage (OCV) or bias voltage. In comparison to the PE one under OCV, the SF intensity is significantly reduced and the peak assigned to the C−H bond shifts to a high wavenumber when introducing LiMMT into the system, indicating that the LiMMT has a preferential effect on the adsorbed behavior of the $Li(DME)_x^+$-FSI^- cluster. With applying the bias voltage of 20 mV, the SF intensity is decreased in the LiMMT-decorated system, while the pristine one keeps the similar intensity, which is attributed to the solvent dissociation from the $Li(DME)_x^+$ cluster since both samples did not show obvious surface morphology changes. Therefore, the above Raman, FTIR, and SFG results clearly depict the LiMMT decoration strongly changes the solvation behaviors of $Li(DME)_x^+$-FSI^- clusters by adsorbing FSI^- anions, propelling the feasible formation of Li^+ for uniform plating.

To further explore practical applications, Figure S19 displays that the Li−Li cell with LiMMT exhibits excellent cycling stability with a stable overpotential of 40 mV and lasts for ∼400 h at 1 mA cm^{-2}. On the contrary, the voltage polarization of the symmetric cell with PE is unstable, caused by the back-and-forth formation of the unstable SEI layer, which is also explained by the increase of charge transfer resistance derived from the electrochemical impedance spectroscopy (EIS) curves (Figure S20).[51] As the test current density increased to 6 mA cm^{-2}, the Li−Li symmetrical cell using the LiMMT separator demonstrates stable cycling and a smooth polarization voltage of 50 mV (Figure S21). Under the current density of 3 mAh cm^{-2}, the cell with LiMMT still stabilizes for a long-term lifespan for 1800 h with a low polarization (Figure 4a), significantly outperforming the symmetric cells with PE. As enlarged in Figure 4b and Figure S22, the cell with the PE separator has a fluctuant voltage hysteresis, accompanied by noisy voltage hysteresis and voltage mutations upon different cycles, while the cell with the LiMMT separator exhibits stable voltage hysteresis within 35 mV.

As anticipated, the full-cells of the Li|single-crystal $LiNi_{0.5}Co_{0.2}Mn_{0.3}O_2$ (NCM523) and Li|$LiFePO_4$ (LFP) were compared. The cell with LiMMT delivers a steady capacity retention of 99.7% over 200 cycles at 1 C (Figure 4c). In contrast, the discharge capacity of the Li|NCM523 cell using the PE separator decays continuously with the cycling accompanied by a significant increase in the overall overpotentials (Figure S23). From the dQ/dV curves in Figure 4d, in comparison with the PE separator, the redox peaks of Li|NCM523 with LiMMT overlap well in successive cycles, while its polarization voltage remains nearly unchanged and reversible, which is attributed to the stable uniform interphase without any dendrite formation. Further, under high loading and lean electrolyte conditions, cells with the LiMMT separator show a super stable cycling tendency compared to that of the PE separator (Figure S24), and it stabilizes at 138.6 mAh g^{-1} after 100 cycles, corresponding to the capacity retention of 100%. Even under the conditions of low salt concentration electrolyte and high cathode loading, the cells using a LiMMT separator still exhibit high reversible capacity with a steady capacity retention (Figure S25), which is close to the level with normal cathode mass loading (Figure 4c). Furthermore, a batch of the handmade level pouch cells has been assembled for real testing (mass loading of 22 mg cm^{-2}, thin Li foil of 50 μm, and electrolyte injection ratio of 2 g Ah^{1-}). The LiMMT separator demonstrates better electrochemical stability than that of the PE separator under such challenging conditions (Figure S26). Similarly, the high-loading Li|LFP cell with a PE separator displays a severe decline after 50 cycles, while the cell with a LiMMT separator remains fairly stable more than 200 cycles at least. The results above reveal that the LiMMT separator has a long lifetime of more than 500 cycles at a high loading of 10 mg cm^{-2}, which is a significant advantage over the previously reported results (Figure 4e and Table S1).

To make sense of the anion-braking effect of LiMMT on plating morphology, the cycled Li metal anodes were subjected to SEM and time-of-flight secondary-ion mass spectrometry (ToF-SIMS) analysis (Figures 5a−5g). Top-SEM and high-resolution SEM images clearly show that a significant quantity of dendritic Li was deposited on the surface of Cu foil as circled when increasing the plating capacity from 1 to 3 mAh cm^{-2} (Figures 5a, 5b, and S27). This incompact structure further leads to an inhomogeneous local electric field distribution and Li ion flux, enhancing the tip effects and dendrite growth. Thus, the loose thickness of 19 μm is generated when plating (Figures S28a and S28b). In contrast, for the LiMMT separator, the surface exhibits a smooth morphology consisting of bulk lithium without Li dendrites. Even with a high capacity of 3 mAh cm^{-2} (Figure 5b), it still presents the flat morphology without any humps. Notably, its thickness is only around 5 μm, which is much less than that of the PE separator (18 μm), demonstrating the dense dendrite-free Li deposition (Figures S28c and S28d). Further, ToF-SIMS is used to analyze the chemical compositions and spatial distribution after cycling. Along with sputtering, the cycled Li metal based on PE separators display strong CH_2^-, LiF_2^-, F^-, and Li^- signals, resulting from the decomposition and reduction of electrolyte components (Figure 5c). However, the species on the PE-decorated Li are randomly distributed with significant aggregations, which should be the crack or dendrite formation when plating (Figure 5e and Figure S29). In the case of the LiMMT separator, the signal rapidly dwindles within 100 s, which is consistent with a reduction in the quantity of electrolyte reaction products (Figure 5d). As displayed in planar mappings, the amount of inorganic matter (F^-) and organic matter (CH_2^-) on the surface of cycled Li is significantly lower than that of the PE separator. In the 3D species reconstruction, obvious cracks are observed in the PE-assisted cell, further confirming that the LiMMT separator played an inhibitory role in both lithium dendrites and infinite occurring side reactions (Figures 5e and 5f).

The kinetic equilibria of ion concentration and current density distribution were further investigated by finite element simulation of COMSOL software. The higher μ_a breaks the electroneutral region under the PE separator (Figure 5h),

where the ion concentration is significantly lower than the bulk concentration (C_0) under the electric field. Worsley, the Li ion distribution at the electrode/electrolyte interface is so much lower that it is likely to increase selective Li deposition, forming a locally concentrated current density distribution environment and aggravating the formation of Li dendrites. During the plating process, more Li ions preferentially deposit around the prominent tip, which is notable for self-amplification with increasing surface roughness and tip electric field strength, resulting in the progressive production of Li dendrites. In contrast, with the LiMMT modification, the concentrated polarization of Li ions is optimized due to the braking effect of anions (Figure 5i). As a result, the Li^+ concentration at the electrode/electrolyte interface is increased, leading to a uniform distribution of Li ions on the anode surface. Moreover, according to the *y*-direction of Li ion concentration along the electrode surface, it is clearly more stable when using a LiMMT separator compared to a PE separator. The temporal evolution of Li plating confirms that LiMMT exhibits smooth surface topography in alleviating the concentration gradient and ensuring the uniform electric field distribution.

Above all, for a better understanding, the significant anion-braking effect is schematically illustrated. Since the commercial PE separator exhibits nonion selectivity (Figure 5j), the anions and cations electro-migrate in opposite directions under the electric field, and the higher μ_a leads to a rapid break of electrical neutrality near the anode surface with a self-generated space charge layer. Eventually, this prompts the self-amplified growth of Li dendrites. However, the designed LiMMT-decorated separator has abundant −OH groups as Lewis acidic sites with electron acceptor capability (Figure 5k), which can restrict the migration of FSI^- anions and effectively decrease the μ_a, realizing the effect of the anion-braking phenomenon. The further optimized Li(solvent)$^+$-anion solvent shell structure helps to dissociate to generate free Li^+ with lower barriers. Additionally, Li ions are enriched at the electrode interface, and the concentration gradient is reduced near the electrode surface, significantly enhancing the reversibility of Li plating/stripping and improving the cycle durability. Thus, it essentially eliminates the self-amplifying growth behavior of Li dendrites and facilitates dense Li deposition.

CONCLUSIONS

In summary, a modified model with an anion-braking effect for regulating Li(solvent)$^+$−anion solvation shell structures for LMBs is pioneeringly designed. Benefiting from its Lewis acid sites and permanent negative charge of the as-domed LiMMT, the functional composite separator has the anion-braking effect of decreasing the μ_a. Thus, the weakened μ_a facilitates a delay in breaking the electroneutrality near the anode, which can reduce the concentration gradient at the anode surface. Further, with the decrease of anions in the solvation shell, the dissociation kinetics of Li(solvent)$^+$ is significantly increased as probed by FTIR, Raman, and SFG, harvesting a smooth dendrite-free surface morphology observed by SEM and ToF-SIMS. Consequently, a consistent long-term Li plating/stripping life (1800 h) is achieved under 3 mAh cm^{-2}, and the high-loading Li-NCM523 and Li-LFP full-cells stabilize for hundreds of cycles with high-capacity retention. The anion-braking composite separator guarantees its easy integration into batteries and provides the general applicability of the anion-braking strategy in a wide range of rechargeable alkali metal batteries such as sodium batteries.

EXPERIMENTAL SECTION

Synthesis of LiMMT and Fabrication of Composite Separators. LiMMT was prepared by exchanging calcium ions in MMT with lithium cations.[52] The MMT was purchased from Aladdin with an average size of 2 μm. The commercial MMT was dispersed in a 1 M solution of lithium chloride. After stirring for 2 days to sufficiently replace calcium cations with lithium cations, the solution was centrifuged and washed three times to separate the LiMMT clay from the supernatant containing impurity ions. Then the LiMMT was dried for 24 h in a vacuum oven at 80 °C. To prepare the LiMMT composite separator, an 80:20 mass ratio of LiMMT and polyvinylidene fluoride (PVDF) binders were mixed in *N*-methyl-2-pyrrolidone (NMP) and then scraped onto one side of a commercial PE separator and dried overnight at 60 °C under vacuum. The loading was about 0.57 mg cm^{-2}.

Materials Characterizations. The microstructure of the composite separator and electrode was examined by scanning electron microscopy (SEM, JEOL JSM-7500FA). The Fourier transform infrared spectra of the samples were recorded by a Thermo Scientific/Nicolet iS50 spectrometer in the wavenumber range of 100−5000 cm^{-1}. X-ray diffraction (XRD) measurements were performed on a Rigaku diffractometer fitted with Cu Kα X-ray (λ = 1.5406 Å) radiation with a scan range from 5° to 80°. X-ray photoelectron spectroscopy (XPS) of the MMT and LiMMT and cycled electrode was performed using a ESCALAB 250Xi spectrometer with Al Kα excitation (1486.6 eV). Time-of-flight secondary-ion mass spectrometry (IONTOF) was utilized to measure cycled lithium surfaces with/without LiMMT. The *in situ* sum frequency generation (SFG) measurements were performed on the commercial picosecond laser. All characterized electrodes were washed with 1,2-dimethoxy-ethan (DME, Sigma-Aldrich, 99%) to defecate electrolyte salts and residual solvents.

Cell Assembly and Electrochemical Measurements. Li/Cu half-cells were assembled in a CR2032-type coin cell, using Cu foil as the working electrode, a Li anode as the counter electrode, and a PE separator and/or LiMMT composite separator as the separator. The electrolyte used for all electrochemical measurements was 60 μL of 6.0 M LiFSI in DME.[53] To prepare the NCM523 and $LiFePO_4$ electrodes, NCM523 or $LiFePO_4$, super-P, and PVDF at a weight ratio of 8:1:1 was mixed in NMP to form a homogeneous slurry and then scraped on an Al foil, respectively. After drying at 90 °C under vacuum for 12 h, the Li|NCM523 and Li|$LiFePO_4$ cells were assembled with a PE separator or LiMMT composite separators. The mass loading of the LFP active materials was about 10 mg cm^{-2}. The mass loading of the NCM523 active materials was about 3 and 15 mg cm^{-2} for regular and higher loading tests, respectively. The Li foil was about 500 μm for the low active materials loading test and 100 μm for the higher active materials loading test. The Li|$LiFePO_4$ cells were galvanostatically cycled between 2.5 and 4.0 V at 1 C. Galvanostatic cycling was performed on the Li|NCM523 cells between 2.8 and 4.3 V at 1 C.

All of the electrochemical properties of cells were performed on the Bio-Logic EC-LAB SP-300 electrochemical workstation. Electrochemical impedance spectroscopy (EIS) was tested at room temperature with a frequency range of 10^6 Hz to 0.01 Hz with an amplitude of 10 mV. The lithium ion transference number (t_{Li^+}) was measured by a combination of AC impedance and DC polarization using symmetric cells with different separators. The initial (I_0) and steady-state (I_s) polarization currents of the cell were recorded at a DC polarization voltage of 10 mV (ΔV). The interface resistance before polarization (R_0) and after polarization (R_s) was tested by AC impedance. Then, using the following eq 3, the lithium ion transference number was determined.[54]

$$t_{Li+} = \frac{I_s(\Delta V - I_0 R_0)}{I_0(\Delta V - I_s R_s)} \quad (3)$$

The instantaneous nucleation with diffusion-controlled growth can be expressed by eq 4:[55,56]

$$\frac{i^2}{i_{max}^2} = 1.9542\left(\frac{t_{max}}{t}\right)\left[1 - \exp\left(-1.2564\frac{t^2}{t_{max}^2}\right)\right]^2 \quad (4)$$

The nucleation density can be calculated using eq 5 below, where F is the Faraday constant, C^{∞} is the concentration of the electrolyte, ρ is the density of lithium metal, z is the number of electrons involved in the reaction, and M is the molar mass of lithium metal:[57]

$$N = 0.065*\left(\frac{zFC^{\infty}}{t_{max}i_{max}}\right)\left(\frac{\rho}{8\pi C^{\infty}M}\right)^{1/2} \quad (5)$$

Simulation of Li Deposition. COMSOL Multiphysics 5.6 was used to simulate the morphology of lithium metal growth with Li^+ concentration distribution and current density distribution at the interface between the anode and electrolyte. The geometry of the model was divided into three sections: the upper region is the lithium metal anode, the middle region is the electrolyte domain, and the lower region is the copper foil cathode. Current sources were imposed on the upper and lower boundaries of the model. The current density was 1.0 mA cm^{-2}, which was in accordance with the experimental setup. The model uses transient calculation to reveal the in situ the reduction process of lithium ions in the negative electrode under discharge conditions. Lithium deposition using commercial separators has a dendritic shape, whereas lithium deposition using LiMMT coated separators is smoother. These two models are based on the ideal model and accurately reflect the actual situation.

Density Function Theory (DFT) Calculations. The (001) crystal plane was obtained by cutting the LiMMT unit cell, and after expanding the cell into a 2 × 2 supercell, a vacuum layer of about 15 Å was established on the surface. Density functional theory (DFT) calculations were performed using CP2K software,[58] PBE functionals with added Crimme D3 dispersion correction[59,60] at the DZVP-MOLOPT-SR-GTH basis set level and Goedecker–Teter–Hutter (GTH) pseudopotentials are used to optimize the structure of the system, and the plane-wave energy cutoff is 600 Ry. On the basis of structure optimization, a larger basis set TZVP-MOLOPT-GTH is used to calculate the single-point energy at 3 × 3 × 1 k-points. VESTA software was used to analyze the images of the calculate results.[61] The binding energies of Li^+ and FSI^- and LiMMT and FSI^- can be described by the following equations, respectively:

$$E_{bind} = E_{Li-FSI^-} - E_{Li^+} - E_{FSI^-}$$

$$E_{bind} = E_{LiMMT-FSI^-} - E_{LiMMT} - E_{FSI^-}$$

AUTHOR INFORMATION

Corresponding Authors

Jian Wang − *i-Lab & CAS Key Laboratory of Nanophotonic Materials and Devices, Suzhou Institute of Nano-tech and Nano-bionics, Chinese Academy of Sciences, Suzhou 215123, P. R. China; Helmholtz Institute Ulm (HIU), Ulm D89081, Germany;* orcid.org/0000-0002-7945-0826; Email: jian.wang@kit.edu

Dong Wang − *Key Laboratory of Automobile Materials of MOE, School of Materials Science and Engineering, and Jilin Provincial International Cooperation Key Laboratory of High-Efficiency Clean Energy Materials, Jilin University, Changchun 130012, P. R. China*; Email: wangdong2023@jlu.edu.cn

Xiaobo Ji − *Hunan Province Key Laboratory of Chemical Power Source, College of Chemistry and Chemical Engineering, Central South University, Changsha 410083, P. R. China;* orcid.org/0000-0002-5405-7913; Email: xji@csu.edu.cn

Xing Ou − *School of Metallurgy and Environment, Central South University, Changsha 410083, P. R. China;* orcid.org/0000-0001-6302-7372; Email: ouxing@csu.edu.cn

Authors

Zibo Zhang − *Hunan Province Key Laboratory of Chemical Power Source, College of Chemistry and Chemical Engineering, Central South University, Changsha 410083, P. R. China; School of Metallurgy and Environment, Central South University, Changsha 410083, P. R. China*

Haozhe Qin − *School of Metallurgy and Environment, Central South University, Changsha 410083, P. R. China*

Bao Zhang − *School of Metallurgy and Environment, Central South University, Changsha 410083, P. R. China*

Hongzhen Lin − *i-Lab & CAS Key Laboratory of Nanophotonic Materials and Devices, Suzhou Institute of Nano-tech and Nano-bionics, Chinese Academy of Sciences, Suzhou 215123, P. R. China*

Weitao Zheng − *Key Laboratory of Automobile Materials of MOE, School of Materials Science and Engineering, and Jilin Provincial International Cooperation Key Laboratory of High-Efficiency Clean Energy Materials, Jilin University, Changchun 130012, P. R. China*

Notes

The authors declare no competing financial interest.

ACKNOWLEDGMENTS

We gratefully acknowledge the financial support from the National Natural Science Foundation of China (52070194, 21972164, and 22279161), the Natural Science Foundation of Hunan Province (2022JJ20069), the National Key R&D Program of China (2021YFA1201503), and the Natural Science Foundation of Jiangsu Province (BK. 20210130), Innovative and Entrepreneurial Doctor in Jiangsu Province (JSSCBS20211428). J.W. acknowledges the funding provided by the Alexander von Humboldt Foundation and the basic funding of the Helmholtz Association. We also thank the technical support from Nano-X, Suzhou Institute of Nano-Tech and Nano-Bionics, Chinese Academy of Sciences.

REFERENCES

(1) Niu, C.; Liu, D.; Lochala, J. A.; Anderson, C. S.; Cao, X.; Gross, M. E.; Xu, W.; Zhang, J.-G.; Whittingham, M. S.; Xiao, J.; Liu, J. Balancing Interfacial Reactions to Achieve Long Cycle Life in High-Energy Lithium Metal Batteries. *Nat. Energy* **2021**, *6*, 723−732.

(2) Albertus, P.; Babinec, S.; Litzelman, S.; Newman, A. Status and Challenges in Enabling the Lithium Metal Electrode for High-Energy and Low-Cost Rechargeable Batteries. *Nat. Energy* **2018**, *3*, 16−21.

(3) Zhang, X. Q.; Chen, X.; Xu, R.; Cheng, X. B.; Peng, H. J.; Zhang, R.; Huang, J. Q.; Zhang, Q. Columnar Lithium Metal Anodes. *Angew. Chem., Int. Ed.* **2017**, *56*, 14207−14211.

(4) Qian, J.; Henderson, W. A.; Xu, W.; Bhattacharya, P.; Engelhard, M.; Borodin, O.; Zhang, J. G. High Rate and Stable Cycling of Lithium Metal Anode. *Nat. Commun.* **2015**, *6*, 6362.
(5) Liu, S.; Liu, X.; Chen, M.; Wang, D.; Ge, X.; Zhang, W.; Wang, X.; Wang, C.; Qin, T.; Qin, H.; Qiao, L.; Zhang, D.; Ou, X.; Zheng, W. High-Density/Efficient Surface Active Sites on Modified Separators to Boost Li-S Batteries via Atomic Co^{3+}-Se Termination. *Nano Res.* **2022**, *15*, 7199−7208.
(6) Ou, X.; Liu, T.; Zhong, W.; Fan, X.; Guo, X.; Huang, X.; Cao, L.; Hu, J.; Zhang, B.; Chu, Y.; Hu, G.; Lin, Z.; Dahbi, M. M.; Alami, J. M.; Amine, K.; Yang, C.; Lu, J. Enabling High Energy Lithium Metal Batteries via Single-Crystal Ni-Rich Cathode Material Co-Doping Strategy. *Nat. Commun.* **2022**, *13*, 2319.
(7) Gu, Y.; Wang, W. W.; Li, Y. J.; Wu, Q. H.; Tang, S.; Yan, J. W.; Zheng, M. S.; Wu, D. Y.; Fan, C. H.; Hu, W. Q.; Chen, Z. B.; Fang, Y.; Zhang, Q. H.; Dong, Q. F.; Mao, B. W. Designable Ultra-Smooth Ultra-Thin Solid-Electrolyte Interphases of Three Alkali Metal Anodes. *Nat. Commun.* **2018**, *9*, 1339.
(8) Wang, J.; Li, L.; Hu, H.; Hu, H.; Guan, Q.; Huang, M.; Jia, L.; Adenusi, H.; Tian, K. V.; Zhang, J.; Passerini, S.; Lin, H. Toward Dendrite-Free Metallic Lithium Anodes: From Structural Design to Optimal Electrochemical Diffusion Kinetics. *ACS Nano* **2022**, *16*, 17729−17760.
(9) Wang, J.; Jia, L.; Zhong, J.; Xiao, Q.; Wang, C.; Zang, K.; Liu, H.; Zheng, H.; Luo, J.; Yang, J.; Fan, H.; Duan, W.; Wu, Y.; Lin, H.; Zhang, Y. Single-Atom Catalyst Boosts Electrochemical Conversion Reactions in Batteries. *Energy Storage Mater.* **2019**, *18*, 246−252.
(10) Hafez, A. M.; Jiao, Y.; Shi, J.; Ma, Y.; Cao, D.; Liu, Y.; Zhu, H. Stable Metal Anode Enabled by Porous Lithium Foam with Superior Ion Accessibility. *Adv. Mater.* **2018**, *30*, No. 1802156.
(11) Wang, S. H.; Yin, Y. X.; Zuo, T. T.; Dong, W.; Li, J. Y.; Shi, J. L.; Zhang, C. H.; Li, N. W.; Li, C. J.; Guo, Y. G. Stable Li Metal Anodes via Regulating Lithium Plating/Stripping in Vertically Aligned Microchannels. *Adv. Mater.* **2017**, *29*, No. 1703729.
(12) Yang, C. P.; Yin, Y. X.; Zhang, S. F.; Li, N. W.; Guo, Y. G. Accommodating Lithium into 3D Current Collectors with a Submicron Skeleton towards Long-Life Lithium Metal Anodes. *Nat. Commun.* **2015**, *6*, 8058.
(13) Lee, J. I.; Shin, M.; Hong, D.; Park, S. Efficient Li-Ion-Conductive Layer for the Realization of Highly Stable High-Voltage and High-Capacity Lithium Metal Batteries. *Adv. Energy Mater.* **2019**, *9*, No. 1803722.
(14) Li, X.; Chu, Z.; Jiang, H.; Dai, Y.; Zheng, W.; Liu, A.; Jiang, X.; He, G. Redistributing Li-Ion Flux and Homogenizing Li-Metal Growth by N-Doped Hierarchically Porous Membranes for Dendrite-Free Lithium Metal Batteries. *Energy Storage Mater.* **2021**, *37*, 233−242.
(15) Zhang, Y.; Wang, G.; Tang, L.; Wu, J.; Guo, B.; Zhu, M.; Wu, C.; Dou, S. X.; Wu, M. Stable Lithium Metal Anodes Enabled by Inorganic/Organic Double-Layered Alloy and Polymer Coating. *J. Mater. Chem. A* **2019**, *7*, 25369−25376.
(16) Cao, C. Y.; Zhou, Y. H.; Ubnoske, S.; Zang, J. F.; Cao, Y. T.; Henry, P.; Parker, C. B.; Glass, J. T. Highly Stretchable Supercapacitors via Crumpled Vertically Aligned Carbon Nanotube Forests. *Adv. Energy Mater.* **2019**, *9*, No. 1900618.
(17) Li, P.; Dong, X.; Li, C.; Liu, J.; Liu, Y.; Feng, W.; Wang, C.; Wang, Y.; Xia, Y. Anchoring an Artificial Solid-Electrolyte Interphase Layer on a 3D Current Collector for High-Performance Lithium Anodes. *Angew. Chem., Int. Ed.* **2019**, *58*, 2093−2097.
(18) Ding, F.; Xu, W.; Graff, G. L.; Zhang, J.; Sushko, M. L.; Chen, X.; Shao, Y.; Engelhard, M. H.; Nie, Z.; Xiao, J.; Liu, X.; Sushko, P. V.; Liu, J.; Zhang, J. G. Dendrite-Free Lithium Deposition via Self-Healing Electrostatic Shield Mechanism. *J. Am. Chem. Soc.* **2013**, *135*, 4450−4456.
(19) Fan, X.; Ji, X.; Chen, L.; Chen, J.; Deng, T.; Han, F.; Yue, J.; Piao, N.; Wang, R.; Zhou, X.; Xiao, X.; Chen, L.; Wang, C. All-Temperature Batteries Enabled by Fluorinated Electrolytes with Non-Polar Solvents. *Nat. Energy.* **2019**, *4*, 882−890.
(20) Jie, Y.; Ren, X.; Cao, R.; Cai, W.; Jiao, S. Advanced Liquid Electrolytes for Rechargeable Li Metal Batteries. *Adv. Funct. Mater.* **2020**, *30*, No. 1910777.
(21) Zhang, J.; You, C.; Lin, H.; Wang, J. Electrochemical Kinetic Modulators in Lithium-Sulfur Batteries: From Defect-Rich Catalysts to Single Atomic Catalysts. *Energy Environ. Mater.* **2022**, *5*, 731−750.
(22) Wang, D.; Liu, Y.; Li, G.; Qin, C.; Huang, L.; Wu, Y. Liquid Metal Welding to Suppress Li Dendrite by Equalized Heat Distribution. *Adv. Funct. Mater.* **2021**, *31*, No. 2106740.
(23) Shin, W. K.; Kannan, A. G.; Kim, D. W. Effective Suppression of Dendritic Lithium Growth Using an Ultrathin Coating of Nitrogen and Sulfur Codoped Graphene Nanosheets on Polymer Separator for Lithium Metal Batteries. *ACS Appl. Mater. Interfaces* **2015**, *7*, 23700−23707.
(24) Lee, H.; Ren, X.; Niu, C.; Yu, L.; Engelhard, M. H.; Cho, I.; Ryou, M. H.; Jin, H. S.; Kim, H. T.; Liu, J.; Xu, W.; Zhang, J. G. Suppressing Lithium Dendrite Growth by Metallic Coating on a Separator. *Adv. Funct. Mater.* **2017**, *27*, No. 201704391.
(25) Chang, Z.; Yang, H.; Pan, A.; He, P.; Zhou, H. An Improved 9 Micron Thick Separator for a 350 Wh/kg Lithium Metal Rechargeable Pouch Cell. *Nat. Commun.* **2022**, *13*, 6788.
(26) Zhao, C. Z.; Chen, P. Y.; Zhang, R.; Chen, X.; Li, B. Q.; Zhang, X. Q.; Cheng, X. B.; Zhang, Q. An Ion Redistributor for Dendrite-Free Lithium Metal Anodes. *Sci. Adv.* **2018**, *4*, No. eaat3446.
(27) Yang, M.; Nan, J.; Chen, W.; Hu, A.; Sun, H.; Chen, Y.; Wu, C. Interfacial Engineering of Polypropylene Separator with Outstanding High-Temperature Stability for Highly Safe and Stable Lithium-Sulfur Batteries. *Electrochem. Commun.* **2021**, *125*, No. 106971.
(28) Croce, F.; Appetecchi, G. B.; Persi, L.; Scrosati, B. Nanocomposite Polymer Electrolytes for Lithium Batteries. *Nature* **1998**, *394*, 456−458.
(29) Tan, L.; Sun, Y.; Wei, C.; Tao, Y.; Tian, Y.; An, Y.; Zhang, Y.; Xiong, S.; Feng, J. Design of Robust, Lithiophilic, and Flexible Inorganic-Polymer Protective Layer by Separator Engineering Enables Dendrite-Free Lithium Metal Batteries with $LiNi_{0.8}Mn_{0.1}Co_{0.1}O_2$ Cathode. *Small* **2021**, *17*, No. 2007717.
(30) Wang, J.; Zhang, J.; Duan, S.; Jia, L.; Xiao, Q.; Liu, H.; Hu, H.; Cheng, S.; Zhang, Z.; Li, L.; Duan, W.; Zhang, Y.; Lin, H. Lithium Atom Surface Diffusion and Delocalized Deposition Propelled by Atomic Metal Catalyst Toward Ultrahigh-Capacity Dendrite-Free Lithium Anode. *Nano Lett.* **2022**, *22*, 8008−8017.
(31) Rosso, M.; Gobron, T.; Brissot, C.; Chazalviel, J.-N.; Lascaud, S. Onset of Dendritic Growth in Lithium/Polymer Cells. *J. Power Sources* **2001**, *97*, 804−806.
(32) Wang, W.; Yuan, Y.; Wang, J.; Zhang, Y.; Liao, C.; Mu, X.; Sheng, H.; Kan, Y.; Song, L.; Hu, Y. Enhanced Electrochemical and Safety Performance of Lithium Metal Batteries Enabled by the Atom Layer Deposition on PVDF-HFP Separator. *ACS Appl. Energy Mater.* **2019**, *2*, 4167−4174.
(33) Zahn, R.; Lagadec, M. F.; Hess, M.; Wood, V. Improving Ionic Conductivity and Lithium-Ion Transference Number in Lithium-Ion Battery Separators. *ACS Appl. Mater. Interfaces* **2016**, *8*, 32637−32642.
(34) Zhou, M.; Liu, R.; Jia, D.; Cui, Y.; Liu, Q.; Liu, S.; Wu, D. Ultrathin Yet Robust Single Lithium-Ion Conducting Quasi-Solid-State Polymer-Brush Electrolytes Enable Ultralong-Life and Dendrite-Free Lithium-Metal Batteries. *Adv. Mater.* **2021**, *33*, No. 2100943.
(35) Li, C.; Liu, S.; Shi, C.; Liang, G.; Lu, Z.; Fu, R.; Wu, D. Two-Dimensional Molecular Brush-Functionalized Porous Bilayer Composite Separators Toward Ultrastable High-Current Density Lithium Metal Anodes. *Nat. Commun.* **2019**, *10*, 1363.
(36) Liao, C.; Wang, W.; Han, L.; Mu, X.; Wu, N.; Wang, J.; Gui, Z.; Hu, Y.; Kan, Y.; Song, L. A Flame Retardant Sandwiched Separator Coated with Ammonium Polyphosphate Wrapped by SiO_2 on Commercial Polyolefin for High Performance Safety Lithium Metal Batteries. *Appl. Mater. Today* **2020**, *21*, No. 100793.
(37) Chen, L.; Sun, Y.; Wei, X.; Song, L.; Tao, G.; Cao, X.; Wang, D.; Zhou, G.; Song, Y. Dual-Functional V_2C MXene Assembly in

Facilitating the Sulfur Evolution Kinetics and Li-Ion Sieving towards Practical Lithium-Sulfur Batteries. *Adv. Mater.* **2023**, *35*, No. 2300771.
(38) Wang, J.; Zhang, J.; Wu, J.; Huang, M.; Jia, L.; Li, L.; Zhang, Y.; Hu, H.; Liu, F.; Guan, Q.; Liu, M.; Adenusi, H.; Lin, H.; Passerini, S. Interfacial ″Single-Atom-in-Defects″ Catalysts Accelerating Li^+ Desolvation Kinetics for Long-Lifespan Lithium Metal Batteries. *Adv. Mater.* **2023**, *35*, No. 2302828.
(39) Li, X.; Guan, Q.; Zhuang, Z.; Zhang, Y.; Lin, Y.; Wang, J.; Shen, C.; Lin, H.; Wang, Y.; Zhan, L.; Ling, L. Ordered Mesoporous Carbon Grafted MXene Catalytic Heterostructure As Li-Ion Kinetic Pump toward High-Efficient Sulfur/Sulfide Conversions for Li-S Battery. *ACS Nano* **2023**, *17*, 1653−1662.
(40) Li, L.; Tu, H.; Wang, J.; Wang, M.; Li, W.; Li, X.; Ye, F.; Guan, Q.; Zhu, F.; Zhang, Y.; Hu, Y.; Yan, C.; Lin, H.; Liu, M. Electrocatalytic MOF-Carbon Bridged Network Accelerates Li^+-Solvents Desolvation for High Li^+ Diffusion toward Rapid Sulfur Redox Kinetics. *Adv. Funct. Mater.* **2023**, *33*, No. 2212499.
(41) Yu, Z.; Wang, H.; Kong, X.; Huang, W.; Tsao, Y.; Mackanic, D. G.; Wang, K.; Wang, X.; Huang, W.; Choudhury, S.; Zheng, Y.; Amanchukwu, C. V.; Hung, S. T.; Ma, Y.; Lomeli, E. G.; Qin, J.; Cui, Y.; Bao, Z. Molecular Design for Electrolyte Solvents Enabling Energy-Dense and Long-Cycling Lithium Metal Batteries. *Nat. Energy* **2020**, *5*, 526−533.
(42) Chazalviel, J. Electrochemical Aspects of the Generation of Ramified Metallic Electrodeposits. *Phys. Rev. A* **1990**, *42*, 7355−7367.
(43) Shan, X.; Morey, M.; Li, Z.; Zhao, S.; Song, S.; Xiao, Z.; Feng, H.; Gao, S.; Li, G.; Sokolov, A. P.; Ryan, E.; Xu, K.; Tian, M.; He, Y.; Yang, H.; Cao, P.-F. A Polymer Electrolyte with High Cationic Transport Number for Safe and Stable Solid Li-Metal Batteries. *ACS Energy Lett.* **2022**, *7*, 4342−4351.
(44) Nan, Y.; Li, S.; Han, C.; Yan, H.; Ma, Y.; Liu, J.; Yang, S.; Li, B. Interlamellar Lithium-Ion Conductor Reformed Interface for High Performance Lithium Metal Anode. *Adv. Funct. Mater.* **2021**, *31*, No. 2102336.
(45) Zeng, T.; Yan, Y.; He, M.; Du, D.; Wen, X.; Zhou, B.; Shu, C. A Single-Ion-Conducting Lithium-Based Montmorillonite Interfacial Layer for Stable Lithium−Metal Batteries. *J. Mater. Chem. A* **2022**, *10*, 23712−23721.
(46) Wang, M.; Li, Y.; Li, S.-Y.; Jia, X.-X.; Nie, B.; Sun, H.-T.; Wang, Y.-Y.; Zhu, J. Lithiophilic Montmorillonite As a Robust Substrate toward High-Stable Lithium Metal Anodes. *Rare Met.* **2023**, *42*, 2157−2165.
(47) Liu, Q.; Chen, Z.; Liu, Y.; Hong, Y.; Wang, W.; Wang, J.; Zhao, B.; Xu, Y.; Wang, J.; Fan, X.; Li, L.; Wu, H. B. Cooperative Stabilization of Bi-Electrodes with Robust Interphases for High-Voltage Lithium-Metal Batteries. *Energy Storage Mater.* **2021**, *37*, 521−529.
(48) Wang, X.; Hua, H.; Peng, L.; Huang, B.; Zhang, P.; Zhao, J. Functional Separator for Promoting Lithium Ion Migration and Its Mechanism Study. *Appl. Surf. Sci.* **2021**, *542*, No. 148661.
(49) Yan, Y.; Kong, Q.-R.; Sun, C.-C.; Yuan, J.-J.; Huang, Z.; Fang, L.-F.; Zhu, B.-K.; Song, Y.-Z. Copolymer-Assisted Polypropylene Separator for Fast and Uniform Lithium Ion Transport in Lithium-Ion Batteries. *Chin. J. Polym. Sci.* **2020**, *38*, 1313−1324.
(50) Zou, Y.; Liu, G.; Wang, Y.; Li, Q.; Ma, Z.; Yin, D.; Liang, Y.; Cao, Z.; Cavallo, L.; Kim, H.; Wang, L.; Alshareef, H. N.; Sun, Y. K.; Ming, J. Intermolecular Interactions Mediated Nonflammable Electrolyte for High-Voltage Lithium Metal Batteries in Wide Temperature. *Adv. Energy Mater.* **2023**, *13*, No. 2300443.
(51) Gaberščček, M. Understanding Li-Based Battery Materials via Electrochemical Impedance Spectroscopy. *Nat. Commun.* **2021**, *12*, 6513.
(52) Kim, S.; Park, S.-J. Preparation and Ion-Conducting Behaviors of Poly(ethylene oxide)-Composite Electrolytes Containing Lithium Montmorillonite. *Solid State Ionics* **2007**, *178*, 973−979.
(53) Lin, L.; Suo, L.; Hu, Y. s.; Li, H.; Huang, X.; Chen, L. Epitaxial Induced Plating Current-Collector Lasting Lifespan of Anode-Free Lithium Metal Battery. *Adv. Energy Mater.* **2021**, *11*, No. 2003709.
(54) Lu, Y. Y.; Tikekar, M.; Mohanty, R.; Hendrickson, K.; Ma, L.; Archer, L. A. Stable Cycling of Lithium Metal Batteries Using High Transference Number Electrolytes. *Adv. Energy Mater.* **2015**, *5*, No. 1402073.
(55) Scharifker, B.; Hills, G. J. E. A. Theoretical and Experimental Studies of Multiple Nucleation. *Electrochim. Acta* **1983**, *28*, 879−889.
(56) Zhang, Z.; Luo, H.; Liu, Z.; Wang, S.; Zhou, X.; Liu, Z. A Chemical Lithiation Induced $Li_{4.4}Sn$ Lithiophilic Layer for Anode-Free Lithium Metal Batteries. *J. Mater. Chem. A* **2022**, *10*, 9670−9679.
(57) Scharifker, B. R.; Mostany, J. Three-Dimensional Nucleation with Diffusion Controlled Growth: Part I. Number Density of Active Sites and Nucleation Rates Per Site. *J. Electroanal. Chem.* **1984**, *177*, 13−23.
(58) Hutter, J.; Iannuzzi, M.; Schiffmann, F.; VandeVondele, J. cp2k: atomistic simulations of condensed matter systems. *WIRES. Comput. Mol. Sc.* **2014**, *4*, 15−25.
(59) Ivanov, B. A.; Tartakovskaya, E. V. Stabilization of Long-Range Magnetic Order in 2D Easy-Plane Antiferromagnets. *Phys. Rev. Lett.* **1996**, *77*, 386−389.
(60) Grimme, S. Semiempirical GGA-Type Density Functional Constructed with a Long-Range Dispersion Correction. *J. Comput. Chem.* **2006**, *27*, 1787−99.
(61) Momma, K.; Izumi, F. VESTA 3 for Three-Dimensional Visualization of Crystal, Volumetric and Morphology Data. *J. Appl. Crystallogr.* **2011**, *44*, 1272−1276.